Seismic Evidence for Magmatic Underplating and Intrusion in Northeast China

Chuansong He

Institute of Geophysics, China Earthquake Administration, Beijing 100081, China

Corresponding author: Chuansong He, email: hechuansong@aliyun.com

Key points:

1. A high-velocity anomaly in the lower crust beneath the Songliao Basin might be related to magmatic underplating.
2. An obvious slight low-velocity anomaly is discovered in the middle crust beneath the Songliao Basin, which may be generated by magmatic intrusion.
3. A low-velocity anomaly at near-surface in the Songliao Basin may be induced by the sedimentary cover.

Abstract:

The origin of the large-scale Mesozoic and Cenozoic volcanism in Northeast China (NE China) and the formation of the Songliao Basin (SB) therein are highly controversial topics in the earth sciences. Moreover, the crustal structure closely associated with these physical phenomena remains unclear. To investigate the crustal structure and deep dynamics, ambient noise tomography is performed in NE China. A total of 127 broadband seismic stations with waveform data lasting one year are employed to extract the dispersion curves of Rayleigh waves. Through surface wave tomography, the Rayleigh wave group velocity distributions at 6–40 s are obtained, and the S-wave velocity structure is determined by the inversion of pure-path dispersion data at depths of 0–60 km. The results reveal a high-velocity anomaly in the lower crust beneath the SB that might be related to magmatic underplating generated by mantle plume upwelling. Furthermore, a low-velocity anomaly at near-surface that may be induced by the sedimentary cover is detected within the SB. Finally, an obvious yet slight low-velocity anomaly is discovered in the middle crust of the SB; this feature may be generated by mantle upwelling or magmatic intrusion.

Key words: Ambient noise tomography, Rayleigh wave velocity, S-wave velocity, magmatic underplating and intrusion, Songliao Basin, NE China.

Plain Language Summary

Recently, seismic studies defined an upwelling mantle plume beneath NE China, which may contribute to the magmatism from the Mesozoic to the Cenozoic and the formation of the Songliao Basin, however, the key evidence in the crust remain unclear. In this study, ambient noise tomography is employed to extract the detailed structure of the crust in NE China. Results reveal vestiges of magmatic intrusion and underplating in the crust beneath the centre of NE

China or the Songliao Basin, which may be associated with the magmatism and the formation of the Songliao Basin in NE China.

1. Introduction

NE China, which constitutes the eastern extent of the Central Asian Orogenic Belt (Xiao et al., 2015; Tang et al., 2018; Wang et al., 2019), generally refers to the region between the Siberian Craton and the North China Craton and is bounded by the early Mesozoic (~230 Ma) Mongol-Okhotsk suture to the north, the Middle Jurassic (~160 Ma) Solonker suture to the south, and the Mesozoic-Cenozoic subducting Pacific plate to the east (Pang et al., 2020; Li et al., 2021). This region has experienced the closures of the Paleo-Asian Ocean and the Mongol-Okhotsk Ocean, the amalgamation of the Xing'an, Songliao, and Jiamusi microcontinental blocks, a series of orogenies, large-scale volcanism from the late Cretaceous to the present, and the formation of the Songliao Basin (SB) in the Mesozoic (Li et al., 2021; Pang et al., 2020).

Generally, the extensive volcanism that occurred from the Mesozoic to the Cenozoic and the formation of the Mesozoic SB in NE China are broadly attributed to the dehydration of a stagnant slab in the mantle transition zone (e.g., Zhao et al., 1994; Maruyama et al., 2009; Zhao et al., 2019; Chen and Faccenda, 2019). However, this notion has been challenged by new findings from seismic investigations (e.g., He et al., 2014, Tang et al., 2014; He and Santosh, 2016; He, 2021). For example, the h-k stacking of receiver functions defined an underplated lower crust beneath the SB that may have been generated by an upwelling mantle plume (He et al., 2014). Subsequent tomographic imaging revealed a Mesozoic vestige of the upwelling mantle plume (Tang et al., 2014; He and Snatosh, 2016), and the common conversion point (CCP) stacking of receiver functions revealed the remnant of an upwelling mantle plume in the upper mantle transition zone (He, 2021). These findings imply that the large-scale volcanism and the formation of the SB in NE China may be related to an upwelling mantle plume (He et al., 2014; He and Santosh, 2016; He, 2021). Nevertheless, more critical and direct evidence in the crust is required to clarify this hypothesis.

The technique of directly cross-correlating the continuous background noise between two stations has been extensively applied to investigate the crustal structure and has greatly advanced the resolution of crustal seismic tomography (e.g., Shapiro et al., 2005; Bensen et al., 2007; Yao et al., 2006; Fang et al., 2009). In recent years, a number of studies have been carried out in NE China utilizing variations of this technique, such as ambient noise tomography (Yang et al., 2019), the joint inversion of ambient noise and receiver functions (Zhu et al., 2019), transdimensional Bayesian ambient noise tomography (Kim et a., 2016), ambient noise adjoint tomography (Liu et al., 2017), and the multimodal inversion of Rayleigh waves from ambient seismic noise (Zhan et al., 2020). However, these researchers did not report any information on the crust that may be linked to an upwelling mantle plume.

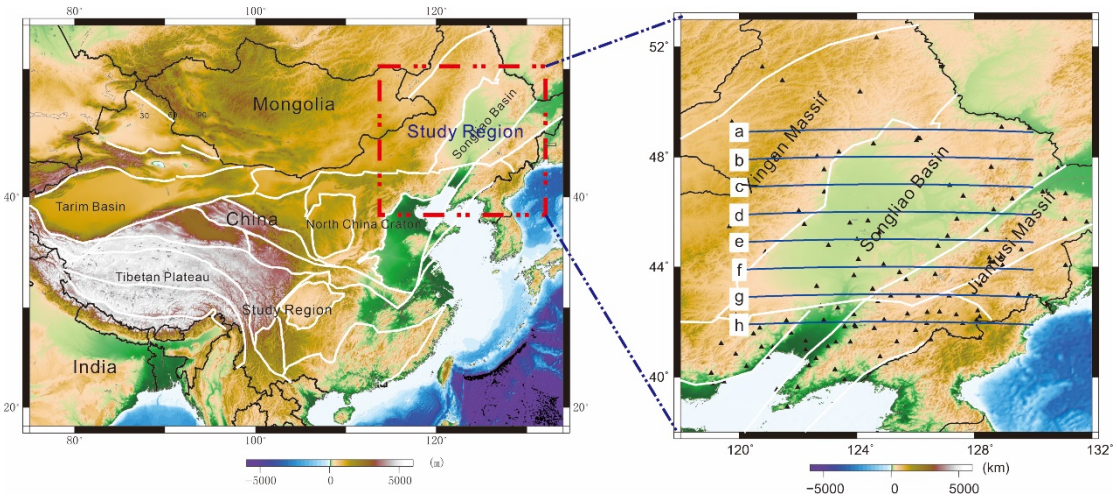

Figure 1. Left panel: location of the study region (red dashed-dotted rectangle). Right panel: green lines: S-wave velocity and S-wave velocity perturbation profiles; black triangles: seismic stations used in this study. White lines in both panels: boundaries of geological units.

In this study, I use high-quality seismic data recorded by the China National Seismic Network across NE China and perform ambient noise tomography (Fig. 1). The results reveal a slight low-velocity anomaly in the middle crust and a high-velocity anomaly in the lower crust beneath the SB that might have been induced by an upwelling mantle plume in the Mesozoic.

1. Data and method

(a) Data and data processing

High-resolution crustal structures can be imaged by directly computing the cross-correlation function of the continuous background noise between any two seismic stations (Campillo and Paul, 2003; Shapiro, 2005; Yao et al., 2006; Bensen et al., 2007; Fang et al., 2010; Lu et al., 2014). In this study, the continuous vertical-component waveforms recorded at 112 seismic stations are collected from the Data Management Center of the China for the period from January 2018 to December 2018. The continuous waveforms are resampled to 5 Hz and cut into daily 24-hour segments (Bensen et al., 2007). Other processing steps are then applied, including removing the instrument response, synchronizing the clock, bandpass filtering (4–50 s), spectral whitening and normalization in the time domain. Finally, the daily waveform at each seismic station is cross-correlated with those at all other seismic stations, and the daily cross-correlation functions for each pair of seismic stations are stacked to produce the final cross-correlation results.

The surface wave signals originating from opposite directions along the path linking two seismic stations can be extracted from the cross-correlations obtained in

the previous step. Because the distribution of ambient noise sources is inhomogeneous, the cross-correlations are asymmetrical. To simplify the data analysis and enhance the signal-to-noise ratio of the surface waves, each cross-correlation is separated into positive and negative lag components, and the so-called symmetric component is obtained by adding the positive and negative components. These symmetric signals are exclusively used in the following analysis.

Based on multiple filtering techniques (Dziewonski, 1969; Levshin et al., 1992) and Computer Programs in Seismology (CPS) software (Herrmann, 2013), the group velocity dispersion curve can be manually picked. If there are n seismic stations, the empirical Green's functions of n(n-1)/2 paths can be extracted. Then, the dispersion curve is quality-controlled to ensure reliable results.

The empirical Green's function is acceptable if the interstation distance is at least 3 times the wavelength at a given period. According to the wavelength and signal-to-noise ratio, the acceptable group velocities are automatically picked (Bensen et al., 2007). Finally, a total of 1810 dispersion curves for the station pairs are obtained from 5253 seismograms containing the Rayleigh wave arrival (Fig. S1).

1. **Rayleigh wave velocity and S-wave velocity inversion**

A generalized 2-D linear inversion procedure, which is a generalization from the classic 1-D method (Backus and Gilbert, 1968) to two dimensions, is employed in the process of surface wave tomography to construct the distribution of the group velocity (Yanovskaya and Ditmar, 1990). According to tests with different damping parameters (=0.1, 0.2 and 0.3), a damping parameter of = 0.2 is selected to achieve the optimal tradeoff between the smoothness of the resulting group velocity images and the fit to the data. A 0.5° × 0.5° lateral grid is designed to be used in the inversion process.

The dispersion curves of the group velocity at each grid node are obtained from the Rayleigh wave group velocity distribution obtained by the above inversion approach. Then, the 1-D S-wave velocity at each grid node is inverted (Herrmann and Ammon, 2004), and the velocities between the nodes are obtained via interpolation. In this way, a 3-D S-wave velocity model is constructed.

The initial model is designed with a constant S-wave velocity of 4.38 km/s from the surface to a depth of 90 km and is divided into 2 km layers to avoid the addition of artificial low-velocity zones. A fixed Vp/Vs ratio of 1.732 is adopted in the inversion process, and the density is extracted from the P-wave velocity (Zanjani et al., 2019).

1. **Resolution analysis**

In this study, the spatially averaged kernel at each grid node in different directions or the average area is used to analyze the resolution and estimate the error (Yanovskaya et al., 2008), where the error can be approximated by an ellipse centered at a point in the 2-D tomographic model. The average area of the ellipse can be calculated based on the smallest and largest axes of the

ellipse. The distribution of the resolution radius indicates that the minimum resolution radius reaches nearly 50 km, while the resolution radius in most of the study area reaches 200 km (Fig. S2), and the spatially averaged resolution radius ranges from 0 to 200 km.

1. **Results**

3.1. Rayleigh wave velocity

Because the group velocities of different periods have different sensitivities to the S-wave velocity at different depths (Urban et al., 1993), the sensitivity kernels of the fundamental Rayleigh wave are obtained from the partial derivatives of the group velocities at different periods. The results indicate that the group velocities of several periods are well resolved at depths ranging from 6 to 40 km (Fig. S3).

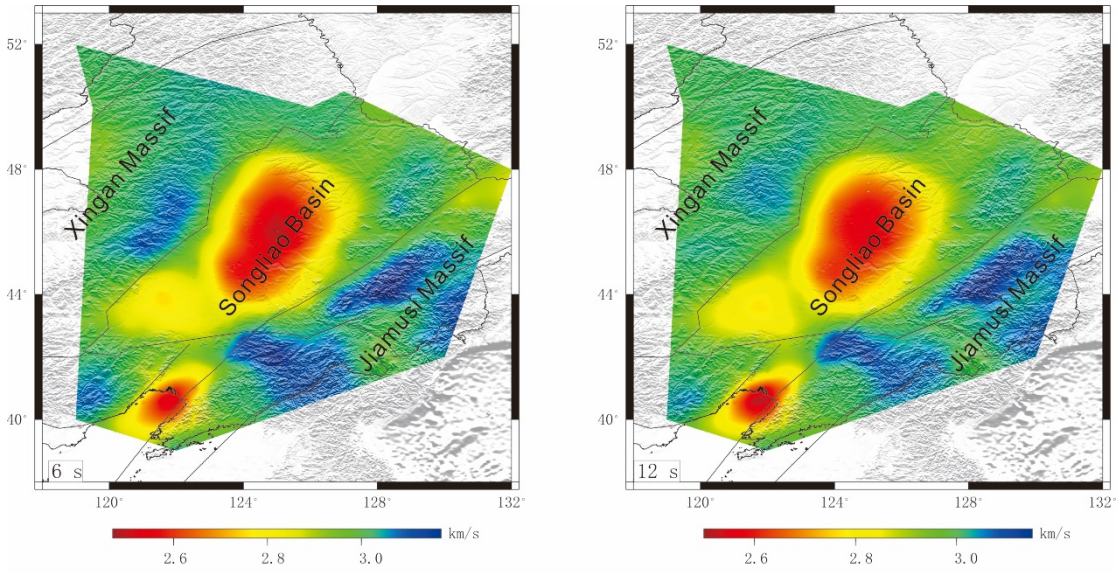
Xingan Massif
Songliao Basin
Jiamusi Massif
6 s
52°
48°
44°
40°
120°
124°
128°
132°
km/s
2.6
2.8
3.0

Xingan Massif
Songliao Basin
Jiamusi Massif
12 s
52°
48°
44°
40°
120°
124°
128°
132°
km/s
2.6
2.8
3.0

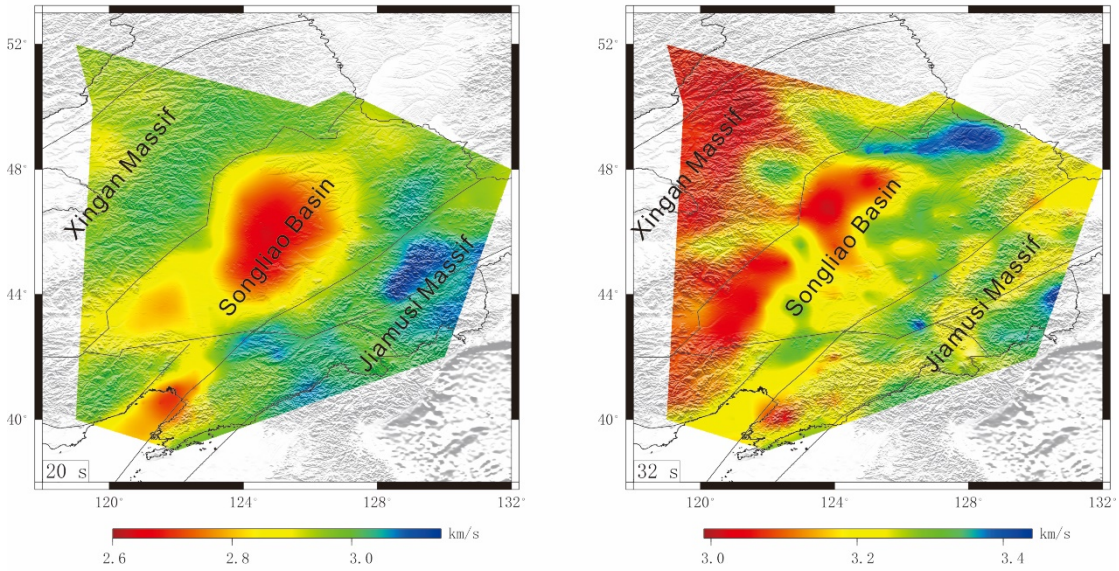
Xingan Massif
Songliao Basin
Jiamusi Massif
20 s
52°
48°
44°
40°
120°
124°
128°
132°
km/s
2.6
2.8
3.0

Xingan Massif
Songliao Basin
Jiamusi Massif
32 s
52°
48°
44°
40°
120°
124°
128°
132°
km/s
3.0
3.2
3.4

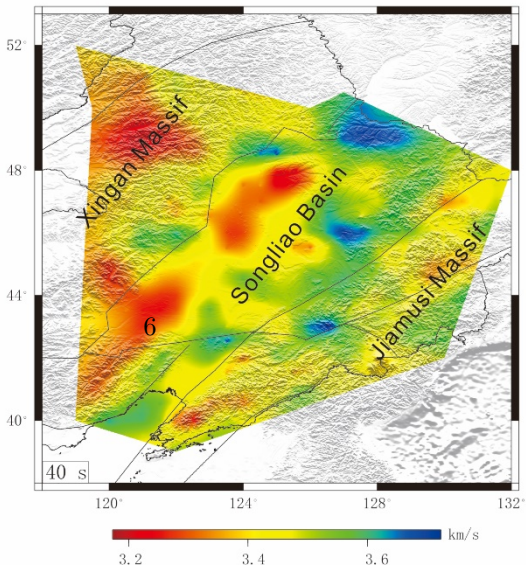
Xingan Massif
Songliao Basin
Jiamusi Massif
6
40 s
52°
48°
44°
40°
120°
124°
128°
132°
km/s
3.2
3.4
3.6

Figure 2. Rayleigh wave group velocities at five different periods. The black lines are the boundaries of geological units.

Due to structural differences at different depths, the group velocity varies of a certain period is most sensitive to the S-wave velocity at 1/3 of the wavelength (Lin et al., 2007; Yang et al., 2007). Here, the representative group velocities at five periods are analyzed (Fig. 2). The Rayleigh wave group velocity of T=6 s reflects the velocity structure mainly within the upper crust, whereas those at T=12 s and 20 s reflect the velocity structure primarily in the middle crust. Similarly, the Rayleigh wave group velocities at medium and long periods (32–40 s) reflect the velocity structure ranging predominantly from the lower crust to the top of the mantle (Fig. 2).

The group velocities at 6–20 s reveal a low-velocity anomaly in the SB and a high-velocity structure in the Jiamusi Massif, whereas those at 32–40 s expose a low-velocity structure in the Xingan Massif and western part of the SB and a high-velocity anomaly in the eastern part of the SB (Fig. 2). Another ambient noise tomography study (Yang et al., 2019) similarly discovered a low-velocity anomaly at 8 s, a minor low-velocity anomaly at 13 s, and a high-velocity anomaly at 21-25 s beneath the SB.

3.2. S-wave velocity structure

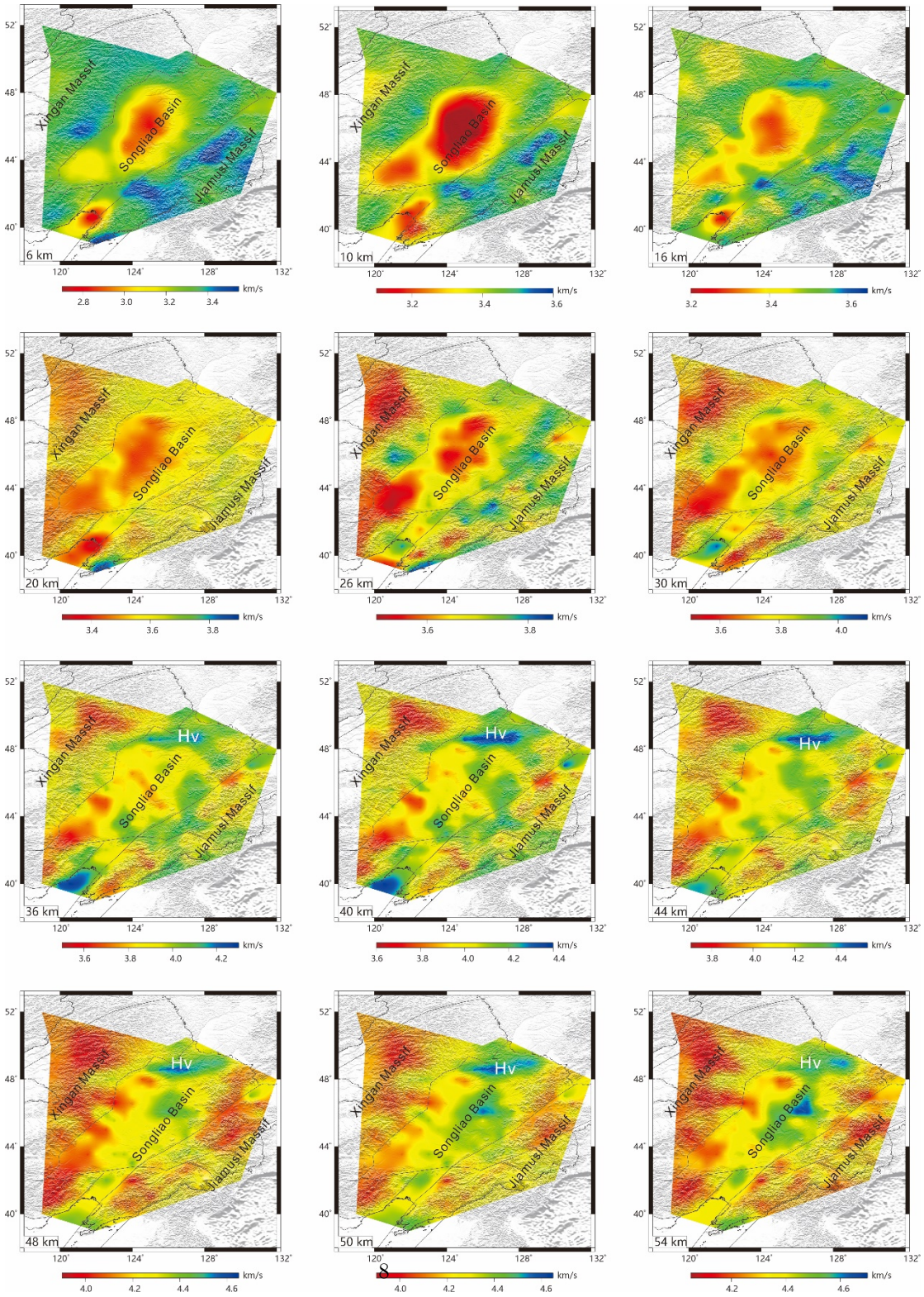
Xingan Massif
Songliao Basin
Jiamusi Massif
Hv
6 km
10 km
16 km
20 km
26 km
30 km
36 km
40 km
44 km
48 km
50 km
54 km
km/s

Figure 3. S-wave velocity distributions at depths of 6-54 km. The black lines are the boundaries of geological units.

A 3-D S-wave velocity model is constructed at depths from 6 km to 54 km following the 1-D S-wave velocity model determined at each grid node (Fig. 3). The results identify a low-velocity anomaly of 2.5 km/s in the SB at a depth of 6 km (Fig. 3), which is consistent with the results of the frequency-dependent P-wave particle motion (Bao and Niu, 2017). Likewise, the joint inversion of surface waves and body waves revealed a low-velocity anomaly at a depth of 5 km (Guo et al., 2018), and noise tomography imaged a low-velocity anomaly at a depth of 4 km beneath the SB (Guo et al, 2016).

A relatively low-velocity anomaly is identified in the SB at depths ranging from 10 km to 30 km, although the S-wave velocity obviously increases from 3.2 km/s to 3.4 km/s from 10 to 30 km (Fig. 3). In contrast, high-velocity structures appear at depths of 6 km, 10 km and 16 km in the Jiamusi Massif and at depths ranging from 20 km to 54 km in the Xingan Massif. A significant high-velocity anomaly appears at the center or southern part of the SB from 36 km to 54 km, and the velocity is anomalously higher at the northern extent of this high-velocity anomaly (Hv) in this depth range (Fig. 3). The multimodal inversion of Rayleigh waves in a previous study also emphasized a large high-velocity zone around the northern edge of the SB at depths of approximately 40–50 km (Zhan et al., 2020). Furthermore, ambient noise adjoint tomography defined a high-velocity anomaly at depths of 35–60 km beneath the SB (Liu et al., 2017). Likewise, the joint inversion of surface waves and body waves identified a high-velocity anomaly at depths of 25–90 km beneath the basin (Guo et al., 2018), and other noise tomography investigations reported high-velocity anomalies beneath the SB at depths of 23–50 (Guo et al, 2016) and 40–50 km (Zhan et al., 2020).

I also calculate the S-wave velocity perturbations at depths of 6–54 km (Fig. S4), and the results are basically consistent with those of the S-wave velocity (Fig. 3).

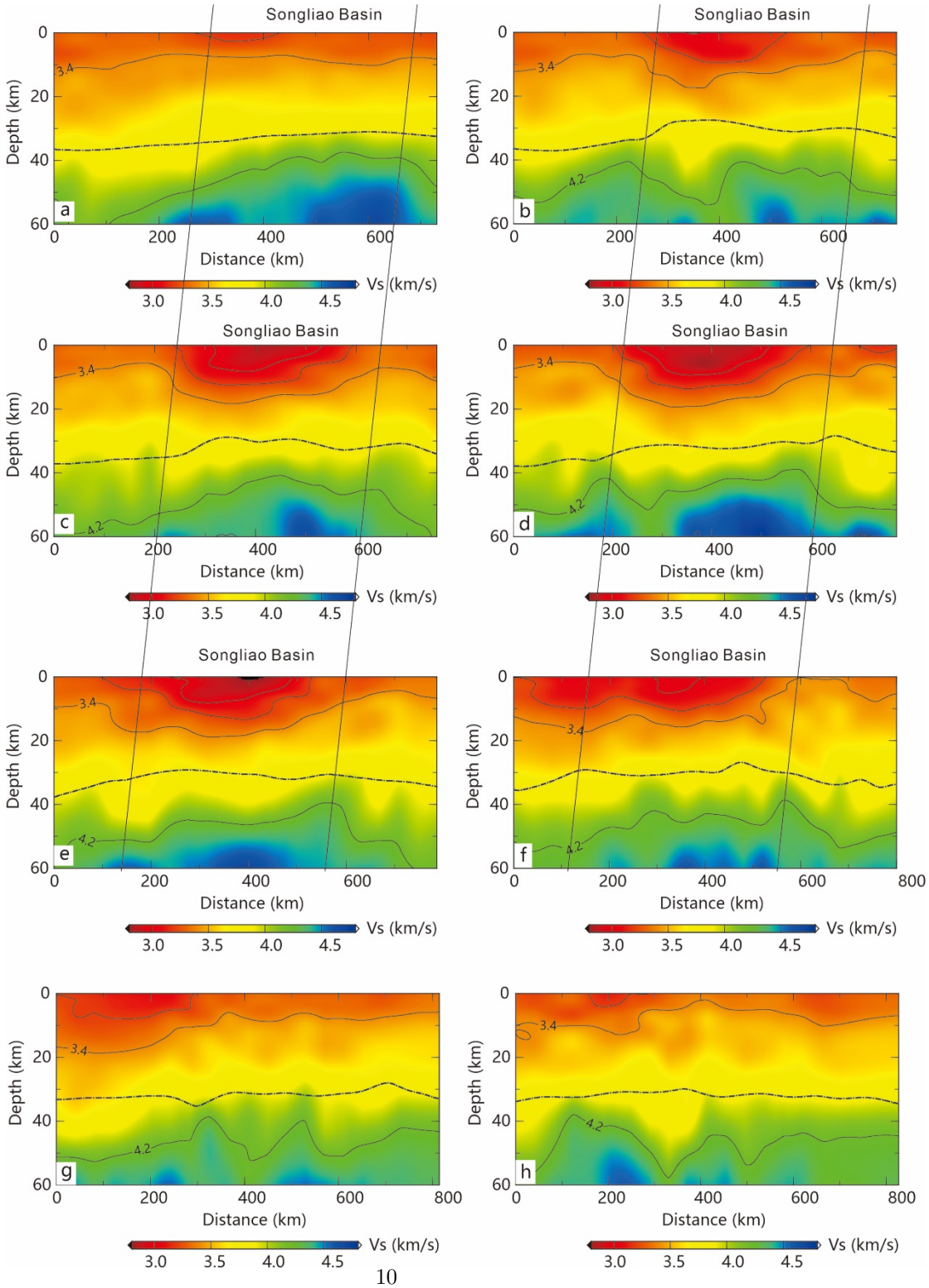
Songliao Basin
Depth (km)
Distance (km)
Vs (km/s)
3.0
3.5
4.0
4.5
3.4
4.2
a
b
c
d
e
f
g
h

Figure 4. S-wave velocity profiles. The velocity boundary of 4.2 km/s is considered the Moho. Green dotted lines: Moho depth inferred from the h-k stacking of receiver functions (He and Santosh, 2016) (Fig. S5, a).

Eight S-velocity profiles pass through or near the SB. If the velocity boundary of 4.2 km/s is considered the Moho, the depths of the Moho obtained by inverting the S-wave structure herein is deeper than those (approximately 10 km) identified by the h-k stacking of receiver functions (Fig. 4; for the locations of the profiles, see Fig. 1). However, the trend of the Moho depth variation determined by S-wave velocity is basically consistent with the trend of that defined by receiver function H-k stacking (Fig. S5, a); for instance, the depth of the Moho beneath the SB is shallower than that of the surrounding regions (Fig. 4). The low-velocity structure of the shallow SB also reflects the thickness (2–6 km) of the sedimentary cover (Fig. 4).

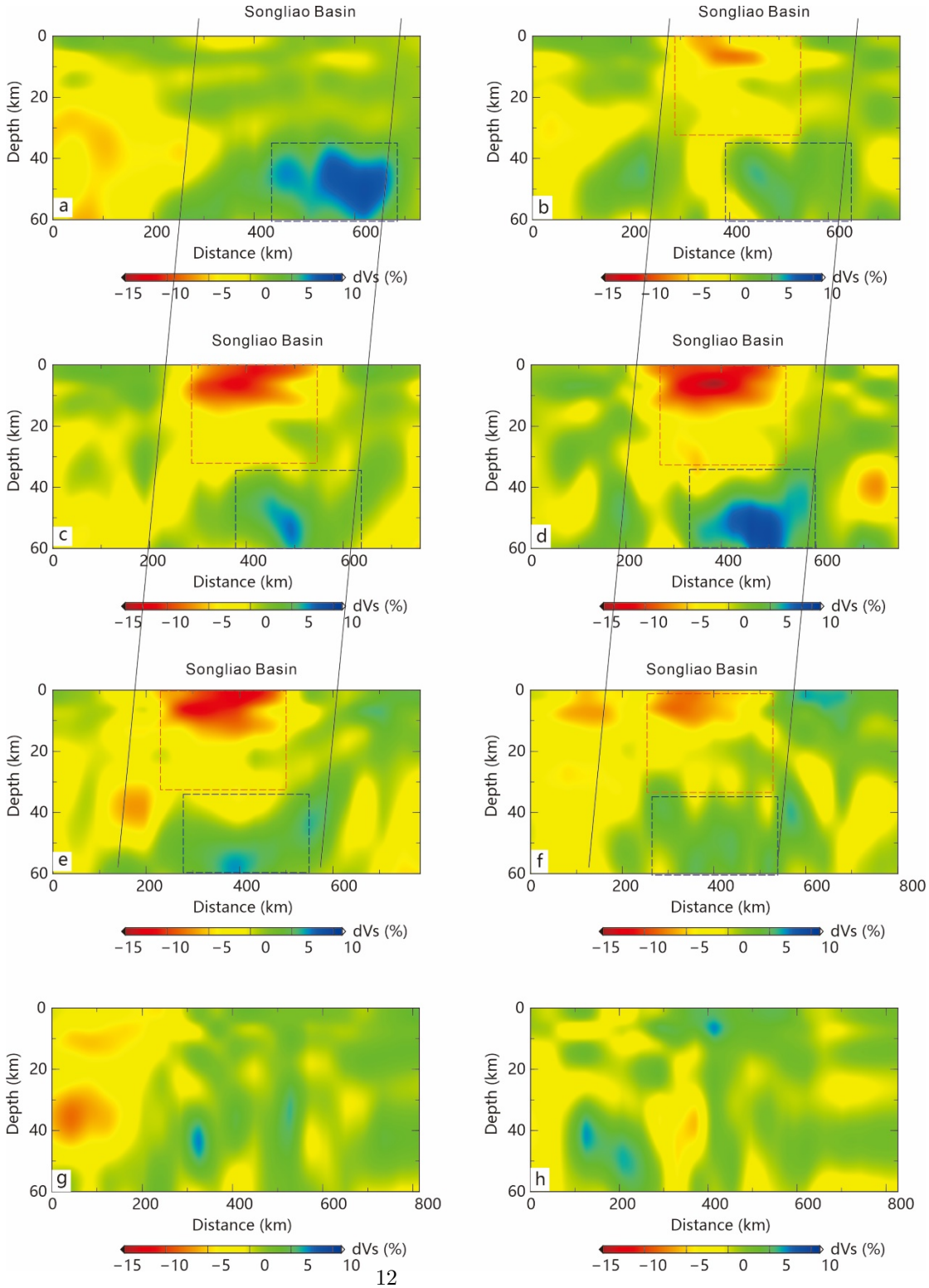
Songliao Basin
Depth (km)
Distance (km)
dVs (%)
a
b
c
d
e
f
g
h

Figure 5. S-wave velocity perturbation profiles.

To further investigate the above results, I establish S-wave velocity perturbation profiles (Fig. 5; for the locations of the profiles, see Fig. 1). The results show high-velocity perturbations at depths of 35–60 km (Fig. 9 a-f, green dashed rectangle) and low-velocity perturbations at depths of 0–30 km beneath the SB; moreover, the low-velocity perturbations at depths of 20–30 km are very slight (Fig. 5 b-f, red dashed rectangle). Previous noise tomography studies similarly reported a minor low-velocity anomaly at a depth of 15 km beneath the SB (Guo et al, 2016; Yang et al., 2019).

1. **Discussion**

(a) **Magmatic underplating**

H-k stacking of receiver functions in the SB region revealed a region of high Vp/Vs ratios in the lower crust of the basin, implying the presence of lower crustal underplating generated by an upwelling mantle plume (He et al., 2014) (Fig. S5, b). Indeed, magmatic underplating can generate a high-velocity anomaly in the lower crust (e.g., Gupta et al., 2010; Jones et al., 2015).

The distributions of the Rayleigh wave velocity, S-wave velocity and S-wave velocity perturbation identified in this study suggest that the lower crust of the SB is a high-velocity structure (Figs. 2–5). Specifically, the S-wave velocity perturbation profiles characterize the crust and mantle at depths of 35–60 km as having a high velocity (Fig. 5 a-f, green rectangle). Based on the rough estimation of the difference in the Moho depths determined from the S-wave velocity structure and h-k stacking of receiver functions, the high-velocity anomaly in the crust might be situated at actual depths of 25–40 km, which is simply the lower crust and the uppermost mantle beneath the SB. These results provide new seismic evidence for lower crustal magmatic underplating in the SB.

4.2. **Magmatic intrusion**

Tomographic studies have reported the presence of a large-scale, mushroom-shaped low-velocity anomaly beneath the SB (Tang et al., 2014; He and Santosh, 2016) (Fig. S6, d, e and f); this anomaly could lead to large mafic magma chambers and magmatic intrusions in the crust and formed low-velocity anomaly (Pirajno, 2007). The S-wave velocity perturbation shows a slight low-velocity anomaly at depths of 20–30 km. Based on the rough estimation of the difference in the Moho depth determined from the S-wave velocity structure and h-k stacking of receiver functions, the slight low-velocity anomaly might be situated at actual depths of approximately 10–20 km, which should be the range of the middle crust. Therefore, it is suggested that the minor low-velocity anomaly in the middle crust beneath the SB may have been generated by a magmatic intrusion induced by an upwelling mantle plume in the Mesozoic.

4.3. Formation of the Songliao Basin

The SB, which covers an area of 26 $\times$ 104 km^2 with a length of 750 km and

a width of 330–370 km (Li et al., 2021), was characterized by episodic rifting and intense volcanism during its early development (Zhang et al., 2011). It has been suggested that a mantle plume beneath NE China initiated continental rifting, which subsequently led to lithospheric extension, intense volcanism and the formation of the SB (He et al., 2014).

The origin and evolution of the Parnaíba Basin of NE Brazil are related mainly to magmatic events (Cardoso et al., 2019). Three magmatic events related to syn-rift I phase of the Parnaíba Basin were also recognized in the Potiguar Basin, also in NE Brazil (Lopes et al., 2018), and these thermal and kinematic processes may be related to the formation of these basins. Lithospheric extension led to the initial mechanical subsidence of the basins, and the subsequent relaxation of the basins might have been linked to thermal subsidence induced by magmatic intrusion (Lipes et al., 2018).

Similarly, it is speculated that an upwelling mantle plume resulted in the initial rifting and mechanical subsidence of the SB; subsequent magmatic intrusions into the crust led to the thermal subsidence of the SB. Moreover, the sedimentary layer in the SB contains volcaniclastic sedimentary rock (Tang et al., 2017), suggesting postmagmatic deposition (Cardoso et al., 2019).

These magmatic intrusions led to a thermal effect, which may be related to the enrichment of oil and gas resources within the basin. There is evidence that the distribution of CO_2 reservoirs is controlled by magmatism (Yu et al., 2019). Furthermore, the thermal subsidence of the SB was punctuated or overprinted by multiple episodes of uplift, which led to the well-known oil-rich Daqing anticline in the SB (Song et al., 2018).

1. Conclusion

The high-velocity anomaly in the lower crust beneath the SB demonstrates that this area experienced magmatic underplating. The slight low-velocity anomaly in the middle crust beneath the SB may be associated with the remnants of magma that was generated by an upwelling mantle plume in the Mesozoic and subsequently intruded into the crust; this plume may have led to the formation of the SB and its subsequent thermal subsidence as well as oil and gas enrichment.

Acknowledgments

We thank the National Key R&D Plan of China (2017YFC601406). The data involved in the cross-correlation can be accessed via https://doi.org/10.5281/zenodo.5574426.

Author contributions

H.C. conducted the analysis, interpreted the results and wrote the manuscript.

Additional information

Competing Interests: The author declares no competing interests.

Electronic supplementary material

Supplementary Information

References

Backus, G. E., & Gilbert, F. (1968). The resolving power of gross Earth data. *Geophysical Journal International,* **16**, 169–205.

Bao, Y., & Niu, F. (2017). Constraining sedimentary structure using frequency dependent P wave particle motion: A case study of the Songliao Basin in NE China. *Journal of Geophysical Research*, **122**, 9083–9094.

Bensen, G. D., Ritzwoller, M. H., Bamin, M. P., Levshin, A. L., Lin, F., & Moschetti, M. P. (2007). Processing seismic ambient noise data to obtain reliable broad-band surface wave dispersion measurements. *Geophysical Journal International*, **169**, 1239–1260.

Campillo, M., & Paul, A. (2003). Long-Range correlations in the diffuse seismic coda. *Science,* **299**, 547-549.

Cardoso, A.R., Nogueira, A. C. R., & Rabelo, C. E. N. (2019), Lake cyclicity as response to thermal subsidence: A post-CAMP scenario in the Parnaíba Basin, NE Brazil. *Sedimentary Geology,* **385**, 96–109.

Ditmar, P. G., & Yanovskaya, T. B. (1987). A generalization of the Backus-Gilbert method for estimation of lateral variations of surface wave velocity. *Izv Akad Nauk SSSR Fiz Zeml (in Russian),* **6**, 30–60.

Dziewonski, A. (1969). A technique for the analysis of transient seismic signals. *Bulletin of the Seismological Society of America,* **59**, 427–444.

Fang, L., Wu, J. & Ding, Z. (2010). High resolution Rayleigh wave group velocity tomography in North China from ambient seismic noise. *Geophysical Journal International,* **181**, 1171–1182.

Guo, Z., Chen, Y. J., Ning, J. Yang, Y., Afonso, J. C., & Tang, Y. (2016). Seismic evidence of on-going sublithosphere upper mantle convection for intraplate volcanism in Northeast China. *Earth and Planetary Science Letters,* **433**, 31–43.

Guo, Z., Wang, K., Yang, Y., Tang, Y., John Chen, Y., & Hung, S. H. (2018). The origin and mantle dynamics of quaternary intraplate volcanism in Northeast China from joint inversion of surface wave and body wave. *Journal of Geophysical Research*, **123**, 2410–2425.

Gupta, S., Santosh, M., & Rai, S. S. (2010). Magmatic underplating of crust beneath the Laccadive Island, NW Indian Ocean. *Geophysical Journal International*, **183**, 536–542.

He, C. (2021), The structure of the upper mantle transition zone beneath northeast China associated with mantle plume migration. *Earth and Space Science*, **8**, e2021EA001874.

He, C. S., Dong, S. W., Chen, X. H., Santosh, M., & Niu, S. Y. (2014), Seismic evidence for plume-induced rifting in the Songliao basin of Northeast China. *Tectonophysics,* **627**, 171–181.

He, C.S., & Santosh, M. (2016). Seismic tomographic evidence for upwelling mantle plume in NE China. *Physics of the Earth and Planetary Interiors,* **254**, 37–45.

Herrmann, R. B. (2013). Computer programs in seismology: An evolving tool for instruction and research. *Seismological Research Letters,* **84**, 1081–1088.

Herrmann, R. B., & Ammon, C. J. (2004). Surface waves, receiver functions, and crustal structure. *Comp. Prog. Seismol. Version* **3.30**.

Jones, E. J. W., McMechan, G. A., & Zeng, X., (2015). Seismic evidence for crustal underplating beneath a large igneous province: The Sierra Leone Rise, equatorial Atlantic. *Marine Geology,* **365**, 52–60.

Kennett, B. L. N., Engdahl, E. R., & Buland, R. (1995). Constraints on seismic velocities in the Earth from traveltimes. *Geophysical Journal International,* **122**, 108–124.

Kim, S., Tkalčić, H., Rhie, J., & Chen, Y. (2016), Intraplate volcanism controlled by back-arc and continental structures in NE Asia inferred from transdimensional Bayesian ambient noise tomography. *Geophysical Research Letters*, **43**, 8390–8398.

Levshin, A., Ratnikova, L., & Berger, J. (1992). Peculiarities of surface-wave propagation across central Eurasia. *Bulletin of the Seismological Society of America,* **82**, 2464–2493.

Li, Z. Q., Chen, J. L., Zou, H., Wang, C. S., Meng, Q. A., Liu, H. L., & Wang, S. Z. (2021). Mesozoic–Cenozoic tectonic evolution and dynamics of the Songliao Basin, NE Asia: Implications for the closure of the Paleo-Asian Ocean and Mongol-Okhotsk Ocean and subduction of the Paleo-Pacific Ocean. *Earth-Science Reviews*, **218**, 103471.

Lin, F. C., Ritzwoller, M. H., Townend, J., Bannister, S., & Savage, M. K. (2007). Ambient noise Rayleigh wave tomography of New Zealand. *Geophysical Journal International* **170**, 649–666.

Liu, Y., Niu, F., Chen, M., & Yang, W. (2017), 3-D crustal and uppermost mantle structure beneath NE China revealed by ambient noise adjoint tomography. *Earth and Planetary Science Letters,* 461, 20–29.

Lopes, J. A. G., de Castro, D. L., & Bertotti, G. (2018). Quantitative analysis of the tectonic subsidence in the Potiguar Basin (NE Brazil). *Journal of Geodynamics,* **117**, 60–74.

Lu, L. Y., He, Z., Ding, Z., & Wang, C. (2014). Azimuthal anisotropy and velocity heterogeneity of Yunnan area based on seismic ambient noise. *Chinese*

Journal of Geophysics (in Chinese with English abstract), **57**, 822–836.

Pang, Y., Guo, X., Zhang, X., Zhu, X., Hou, F., Wen, Z., & Han, Z. (2020). Late Mesozoic and Cenozoic tectono-thermal history and geodynamic implications of the Great Xing'an Range, NE China. *Journal of Asian Earth Sciences,* **189**, 104155.

Pirajno, F. (2007). Ancient to modern earth: the role of mantle plume in the making of continental crust: Earth's Oldest Rocks, edited by Kranendonk, M.J.V., Smithies, R.H., and Bennett, V.C., *Developments in Precambrian Geology*, v.15 (K.C. Condie, Series Editor), DOI: 10.1016/S0166-2635(07)15083-0.

Shapiro, N. M., Campillo, M., Stehly, L., & Ritzwoller, M. H. (2005), High resolution surface wave tomography from ambient seismic noise. *Science,* **307**, 1615–1618.

Song, Y., Stepashko, A., Liu, K., He, Q., Shen, C., Shi, B., & Ren, J. (2018). Post-rift tectonic history of the Songliao Basin, NE China: Cooling events and post-rift unconformities driven by orogenic pulses from plate boundaries. *Journal of Geophysical Research*, **123**, 2363–2395.

Tang, H., Kong, T., Liu, X., Yang, D., Huo, H., & Huang, Y. (2017). Formation mechanism of high-quality reservoirs of Lower Cretaceous volcaniclastic sedimentary rocks in Songliao Basin. *Petroleum Research,* **2**, 186e198.

Tang, J., Xu, W. L., Wang, F., & Ge, W.C. (2018). Subduction history of the Paleo-Pacific slab beneath Eurasian continent: Mesozoic-Paleogene magmatic records in Northeast Asia. *Science China-D,* **61**, 527–559.

Tang, Y., Obayashi, M., Niu, F., Grand, S. P., Chen, Y. J., Kawakatsu, H., Tanaka, S., Ning, J., & Ni, J. F. (2014). Changbaishan volcanism in NE China linked to subduction-induced mantle upwelling. *Nature Geoscience*, **7**, 470.

Urban, L., Artur, C., & Franco, V. (1993). Computation of analytical partial derivatives of phase and group velocities for Rayleigh waves with respect to structural parameters. *Studia Geophysica et Geoddaetica,* **37**, 14–36.

Wang, F., Xu, W. L., Xing, K. C., Wang, Y. N., Zhang, H. H., Wu, W., Sun, C. Y., & Ge, W. C. (2019). Final closure of the Paleo-Asian Ocean and onset of subduction of Paleo-Pacific Ocean: constraints from early Mesozoic magmatism in central southern Jilin Province, NE China. *Journal of Geophysical Research*, **124**, 2601–2622.

Xiao, W. J., Windley, B. F., Sun, S., Li, J. L., Huang, B. C., Han, C. M., Yuan, C., Sun, M. & Chen, H. L. (2015). A tale of amalgamation of three Permo-Triassic collage systems in Central Asia: Oroclines, sutures, and terminal accretion. *Annually Review of Earth and Planetary Sciences,* **43**, 477–507.

Yang, Y., Lei, J., Ai, Y., Zhang, G., Sun, C., Fan, E., Li, L., Mi, Q., Lu, M., He, J., Wang, J., Du, M., Zhang, B., Tian, F., Ma, C., & Liu, Z. (2019). Crustal

structure beneath Northeast China from ambient noise tomography. *Physics of the Earth and Planetary Interiors,* **293**, 106257.

Yang, Y., Ritzwoller, M. H., Levshin, A. L., & Shapiro, N. M. (2007). Ambient noise Rayleigh wave tomography across Europe. *Geophysical Journal International,* **168**, 259–274.

Yanovskaya, T. B., & Ditmar, P. G. (1990), Smoothness criteria in surface-wave tomography. *Geophysical Journal International,* **102**, 63–72.

Yanovskaya, T., B., Kozhevnikov, V. M., Solovei, O. A., & Akchurin, K. R. (2008). Structure of the upper mantle in Asia from phase and group velocities of Rayleigh waves. *Izv. Phys. Solid Earth,* **44**, 622–630.

Yao, H., Van der Hilst, R. D., & de Hoop, M. V., (2006). Surface-wave array tomography in SE Tibet from ambient seismic noise and two-station analysis-I. Phase velocity maps. *Geophysical Journal International,* **166,** 732–744.

Yu, Y., Niu, W., Yang, G., Niu, M., Ma, S., & Tian, L. (2019). Mechanisms for the accumulation of deep gas in the southern Songliao Basin, China. *Journal of Petroleum Science and Engineering,* **182**, 106302.

Zhan, W., Pan, L., & Chen, X., (2020). A widespread mid-crustal low-velocity layer beneath Northeast China revealed by the multimodal inversion of Rayleigh waves from ambient seismic noise. *Journal of Asian Earth Sciences,* **196**, 104372.

Zhang, F. Q., Chen, H. L., Yu, X., Dong, C. W., Yang, S. F., Pang, Y. M., & Batt, G. E. (2011). Early Cretaceous volcanism in the northern Songliao Basin, NE China, and its geodynamic implication. *Gondwana Research,* **19**, 163–176

Zanjani, A. A., Zhu, L., & Herrmann, R. B. (2019). Crustal Structure beneath the Wabash Valley Seismic Zone from the Joint Inversion of Receiver Functions and Surface-Wave Dispersion: Implications for Continental Rifts and Intraplate Seismicity. *Journal of Geophysical Research,* **124,** 7028–7039.

Zhu, H., Tian, Y., Zhao, D., Li, H., & Liu, C. (2019). Seismic structure of the Changbai intraplate volcano in NE China from joint inversion of ambient noise and receiver functions. *Journal of Geophysical Research*, **124**, 4984–5002.